Macromolecules
ARTICLE

Macromolecules **2010**, *43*, 393–401 **393**
DOI: 10.1021/ma9019587

Crystallization of Defect-Free Polyethylene within Block Copolymer Mesophases

Sasha B. Myers[†] **and Richard A. Register***

Department of Chemical Engineering, Princeton University, Princeton, New Jersey 08544-5263. [†]*Current address: 3M Corporate Research Process Laboratory, St. Paul, MN 55144*

Received September 2, 2009; Revised Manuscript Received November 1, 2009

ABSTRACT: We report the morphology and orientation of the crystals which form within the microdomain structures of diblock copolymers of linear polyethylene and glassy poly(vinylcyclohexane), LPE/PVCH, across the spherical, cylindrical, and lamellar morphologies. Compared with short-branched polyethylene (such as hydrogenated polybutadiene), confinement of LPE within spheres, within cylinders, or between PVCH cylinders directly limits the crystal thickness and thereby the crystal melting point. Conversely, crystals formed within LPE lamellae are stacked orthogonally to the LPE/PVCH microdomain layering, so there is no direct limitation imposed on crystal thickness by confinement. As with LPE homopolymer, LPE crystals within lamellae thicken when annealed below the melting point, ultimately forming crystals whose thickness is significantly larger than their lateral extent, set by the bounding PVCH layers. The ribbon-like crystals which form within LPE cylinders or lamellae have a strong orientational coupling to the microdomains; prealignment of the cylindrical or lamellar mesophase by extensional flow yields macroscopic specimens with pronounced *b*-axial and *a*-axial orientations, respectively, after subsequent quiescent crystallization.

Introduction

Confinement of polymer crystallites between or within block copolymer microdomains provides an exceptional opportunity for their manipulation and study.[1−3] For example, confinement within spheres severely restricts the lateral extent of the crystallites and greatly modifies the crystallization kinetics, since each sphere must be individually and homogeneously nucleated to crystallize.[4−6] More subtly, confinement within or between cylinders, or within lamellae, can orient the unit cell relative to the microdomains.[2,7,8] Crystallization of orthorhombic polyethylene (PE) within or between cylinders orients the *b*-axis (fast growth axis) parallel to the cylinder axes, where crystal growth is relatively unhindered;[9] crystallization within lamellae also keeps the *b*-axis in the plane of the lamellae, while the *c*-axis orients parallel to the lamellar interface to eliminate the need for commensurability between the lamellar thickness and crystallite repeat distance, thereby producing an *a*-axial texture.[10,11] Consequently, crystallization of PE within prealigned block copolymers can produce macroscopic specimens with *a*-axial or *b*-axial textures to complement the usual *c*-axial texture produced by fiber spinning.

Many of these effects were uncovered and examined using polymers where the crystallizable block is a low-crystallinity PE, formed by hydrogenation of low-vinyl polybutadiene prepared via anionic polymerization (hPBd).[1,10−13] PE has an extensive characterization literature[14] and numerous practical advantages: excellent thermal stability, rapid crystallization above room temperature, and a convenient freezing point at which the complementary amorphous blocks can be either glassy[13,15] or rubbery.[16] Moreover, anionic polymerization lends itself to block copolymer synthesis, and the two-step route to hPBd allows macromolecular characterization via the unsaturated, soluble PBd precursor. However, a significant shortcoming of this approach is that the 1,2 units in PBd (present at a minimum of 6%) lead to ethyl branch defects in the hPBd, which limit the polymer's crystallinity and restrict the average crystal thickness to ~5 nm.[13,15] Since this thickness is below the microdomain width in typical block copolymers, hPBd crystals do not experience confinement in the thickness direction, as evidenced by the near-constancy of the melting temperature T_m in the presence or absence of confinement.[15] Also, the relatively low crystallinity of hPBd largely negates any effect of confinement on crystallinity, which remains ≈30% whether in homopolymer or block copolymer.[15] The large amorphous content may also moderate the degree of orientational coupling between the crystallites and the microdomains. To explore these possibilities, it would be desirable to replace the hPBd block with a linear polyethylene block (LPE, also known as high-density polyethylene, HDPE), retaining all of the advantages of hPBd while allowing for the formation of relatively thick crystals and a higher degree of crystallinity.

Recently, we have developed a synthetic route to polymers combining LPE blocks with blocks synthesized by anionic polymerization.[17] In brief, ring-opening metathesis polymerization (ROMP) is used to synthesize polycyclopentene (PCP, also known as "polypentenamer"). The ROMP reaction is terminated by vinylbenzaldehyde, placing a styryl group at the end of the PCP which can then be metalated and used to initiate anionic polymerization of monomers such as styrene. In a previous report,[17] we demonstrated this approach by synthesizing a range of PCP/polystyrene (PS) diblocks. Subsequent hydrogenation of the PCP yields defect-free LPE, while hydrogenation of PS yields PVCH (poly(vinylcyclohexane)). Here, we report on the morphology of these LPE/PVCH diblocks: that confinement of defect-free crystalline blocks can lead to direct control of the crystal thickness and melting point; that tight orientational coupling can be achieved between the crystals and cylindrical and lamellar microdomains in these higher-crystallinity

---

*Corresponding author. E-mail: register@princeton.edu.

materials; and that crystals confined within lamellae can nevertheless thicken upon annealing, as in LPE homopolymer, up to values which greatly exceed the widths of the confining lamellae.

Experimental Section

Synthesis. Details of the synthesis of PCP/PS diblocks by ROMP-to-anionic polymerization transformation have been presented previously.[17] The "Schrock-type" catalyst 2,6-diisopropylphenylimidoneophylidenemolybdenum(VI) bis(*tert*-butoxide) was used to polymerize cyclopentene to a desired molecular weight, following the reaction kinetics previously established.[18] ROMP was terminated by the addition of a large excess (10 equiv) of 3-vinylbenzaldehyde. The end-functional PCP was isolated and then metalated with a modest excess of *sec*-butyllithium (*s*BuLi); styrene was then added and polymerized to essential completion. For the precursors to LPE/PVCH 6/42, 15/23, and 28/26, 25 vol % THF was added to the cyclohexane solvent used in the metallation step; 2.5 equiv of *s*BuLi was employed, and 30 min was allowed to elapse prior to styrene addition, to decompose the excess *s*-BuLi and prevent the formation of homopolystyrene.[17] The precursor to LPE/PVCH 10/27 was synthesized similarly, but with 10 vol % THF, 4 equiv of *s*BuLi, and 60 min allowed between metallation and styrene addition. For the precursors to LPE/PVCH 15/18, 19/10, and 25/7, only 1% THF was employed; consequently, homopolystyrene was formed concurrently, of the same molecular weight as the PS block in the diblock. For all diblocks, solvent/nonsolvent fractionation from toluene/methanol was employed to remove any star polymer (formed by addition of a PCP macromer during metallation),[17] and any homopolystyrene, prior to hydrogenation. As previously detailed,[17] compositions of the PCP/PS diblocks were determined by ^{1}H NMR, and molecular weights and polydispersities were determined by gel permeation chromatography (GPC) in THF. The true PCP block number-average molecular weight M_n was obtained by correcting the GPC result for the hydrodynamic volume difference between PCP and the PS calibrants, and the diblock M_n was determined from the PCP block M_n and the ^{1}H NMR composition. Hydrogenation of the PCP/PS diblocks to LPE/PVCH was carried out in a stirred Parr reactor, in cyclohexane at 0.5 wt % polymer, over palladium catalyst supported on calcium carbonate ($Pd^0/CaCO_3$, Pd^0 content 5 wt %, Alfa Aesar; approximately 1:20 ratio of Pd^0 to polymer). A minimum of 400 psig hydrogen was employed, at 100 °C. Hydrogenation was continued for 3−7 days until the *trans* C=C double bond stretch at 966 cm^{-1} in the infrared spectrum was reduced to baseline, which corresponds to $>99.95\%$ saturation of the PCP block. Molecular weights and compositions for the LPE/PVCH diblocks were calculated from those for the PCP/PS precursors assuming complete hydrogenation (+2.016 g per mol double bonds).

Thermal and Morphological Characterization. Differential scanning calorimetry (DSC) measurements were made on heating at 10 °C/min, on ca. 10 mg specimens, with a Perkin-Elmer DSC 7 equipped with a Type II intracooler, calibrated with indium and mercury. Unless otherwise stated (as when the specimens were annealed isothermally to thicken the crystals), specimens were simply cooled from the melt (150 °C) to 20 °C at 10 °C/min and then immediately reheated to determine the peak melting temperature T_m and enthalpy of fusion. Wide- and small-angle X-ray scattering (SAXS and WAXS) employed three different systems, all run from PANalytical PW3830 generators with long fine focus Cu X-ray tubes to yield Cu Kα radiation. All data were collected in transmission, and each system was equipped with its own hot stage. For isotropic specimens, one-dimensional (1D) SAXS measurements employed a slit-collimated Anton-Paar compact Kratky camera and MBraun OED-50M position-sensitive detector. Data were corrected for detector sensitivity and positional linearity, empty beam scattering, and sample thickness and transmittance, placed on an absolute intensity scale via a polyethylene standard, and desmeared for slit length.[19] Intensities are presented against the magnitude of the momentum transfer vector $q = (4\pi/\lambda) \sin \theta$, where θ is half the scattering angle; calibration was via a silver behenate[20] standard (d = 5.838 nm). For oriented specimens, two-dimensional (2D) SAXS and WAXS measurements were conducted. 2D SAXS measurements employed a custom-designed point-collimation system of the "DuMond geometry",[21] which focuses the X-ray beam in the vertical and horizontal directions by two bent Si (111) triangular crystals (Molecular Metrology, Northampton, MA; now Rigaku USA). Double-crystal monochromatization provides exceptional wavelength resolution, as it passes only the Cu Kα_1 line. Scattered X-rays are collected by a Molecular Metrology 2D argon-filled Gabriel-type[22] multiwire detector situated 1.5 m downstream from the sample position. The sample chamber and optical train are evacuated to minimize scattering and absorption by air; transmitted X-ray intensity is monitored by a photodiode in the beamstop. Data were corrected for detector sensitivity, empty beam scattering, sample transmittance, and specimen thickness, with the scattering angle and absolute intensity calibrated as for the 1D SAXS system. 2D WAXS measurements employed a Statton pinhole camera system previously described,[23] using Kodak image plates read by a GE Biosciences Storm 820 scanner. The isotropic two-dimensional patterns were converted to one-dimensional traces of intensity vs scattering angle 2θ, calibrated with NaCl. Aligned specimens of cylinder- and lamella-forming diblocks were prepared by planar extensional flow in a lubricated channel die.[24,25] Atomic force microscopy phase images were acquired with a Digital Instruments (now Veeco) Dimension 3000 AFM equipped with a Nanoscope IIIa controller and a Digital Instruments "beta" prototype hot stage, in tapping mode using Si tips (Veeco) resonating at 300 kHz. Specimens were prepared by spin-coating from a 1 wt % polymer solution in toluene onto a Si wafer at 1000−2000 rpm. To prevent premature crystallization of the LPE block, the solution was heated to ≈80 °C and spun onto a heated wafer and chuck. Films were annealed offline at 150 °C for 30−60 min prior to AFM imaging to ensure the development of microphase-separated structure.

Results and Discussion

Diblock and Crystallite Morphology. Key molecular characteristics of the LPE/PVCH diblocks are listed in Table 1. For convenience, materials will be denoted throughout as "LPE/PVCH x/y", where x and y are the approximate molecular weights of the LPE and PVCH blocks in kg/mol. All materials are characterized by a narrow molecular weight distribution (diblock PDI ≈ 1.1).

All of the diblocks discussed herein form microphase-separated melts, and since the glass transition temperature T_g of PVCH exceeds the crystallization temperature of LPE, the overall microdomain structure is retained upon crystallization.[13,15] Figure 1 demonstrates the relative positions of the PVCH T_g and the LPE melting point, T_m, in LPE/PVCH 6/42, where the two transitions are well separated. Figure 2 demonstrates an example of how the overall microdomain morphology in these LPE/PVCH diblocks is retained upon crystallization, by presenting AFM phase images of an LPE/PVCH 10/27 thin film (40 nm thick by ellipsometry). This polymer forms cylinders of LPE in bulk; in the thin film of Figure 2, the cylinder axes are oriented perpendicular to the film surface, a consequence of the similar surface energies of the two blocks.[26] After heating into the melt and cooling to 120 °C (Figure 2a), the cylinders of molten LPE are visible as dark circles due to their lower modulus relative to the glassy PVCH matrix. After further cooling to room temperature

Table 1. Molecular and Morphological Characteristics of LPE/PVCH Diblocks

LPE/ PVCH	w_{LPE}	LPE M_n (g/mol)	LPE PDI	diblock PDI	melt q^* (nm^{-1})	morphology	melt D_S, D_C, or L_E (nm)	peak T_m (°C)	$w_{c,\mathrm{LPE}}$	t_c (nm)	D_x, W_x (nm)
6/42	0.124	6 000	1.09	1.06	0.255	$\mathrm{SPH_{LPE}}$	17.9	117.2	0.395	6.7	13.6
10/27	0.274	10 300	1.08	1.08	0.200	$\mathrm{CYL_{LPE}}$	21.1	120.6	0.401	9.2	12.6
15/23	0.399	15 300	1.08	1.08	0.163	$\mathrm{CYL_{LPE}}$	30.9	127.9	0.609	13.3	28.4
15/18	0.457	15 300	1.08	1.08	0.233	LAM	13.4	126.9	0.632	13.8	[13.4][a]
28/26	0.520	28 200	1.14	1.12	0.111	LAM	31.7	128.7	0.620	14.0	[31.7][a]
19/10	0.655	18 800	1.09	1.09	0.201	LAM	21.6	127.2	0.627	13.0	[21.6][a]
25/7	0.777	25 300	1.08	1.08	0.222	$\mathrm{CYL_{PVCH}}$	15.2	130.4	0.743	14.6	[b]

[a] Set equal to the upper bound of $W_x = L_E$; the value of t_c so determined is therefore a lower bound. [b] Assumed unconstrained ($1/W_x = 0$, final term in eq 2b dropped).

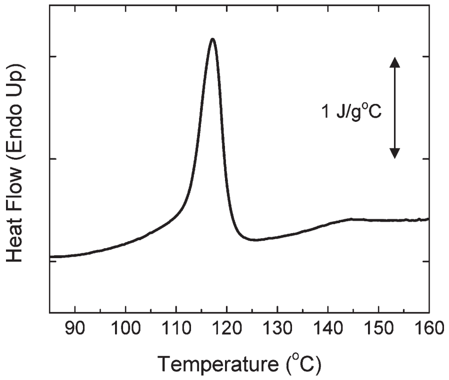

Figure 1. DSC thermogram of LPE/PVCH 6/42 upon heating at 10 °C/min. The melting endotherm of the LPE spheres (peak T_m = 117.2 °C) and the glass transition of the PVCH matrix (135 °C) are clearly evident.

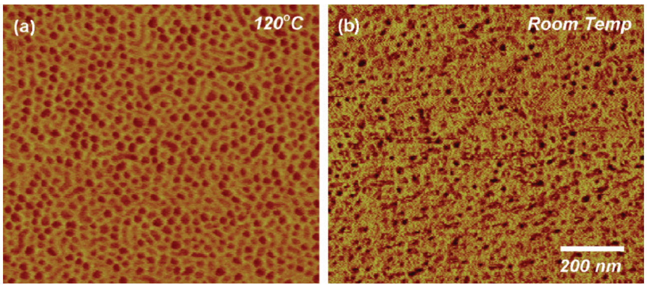

Figure 2. AFM phase images of LPE/PVCH 10/27 spun onto a Si wafer, forming vertical cylinders. Bright (yellow) domains are hard (glassy PVCH or crystalline LPE), while dark (brown) domains are soft (amorphous LPE). (a) Image at 120 °C after cooling from the melt; no crystals present. (b) Image at room temperature after cooling from the melt. Different regions of the film are covered in the two images.

(Figure 2b), the overall domain structure is preserved; moreover, a bright spot is visible in the center of many of the circles, reflecting an LPE crystal within the domain.

Figure 3 shows SAXS patterns, both in the melt and the solid state, for polymers exhibiting a morphology consisting of spheres of LPE (Figure 3a), cylinders of LPE (Figure 3b), and alternating lamellae (Figure 3c). The patterns taken in the melt (red curve in each set) show a narrow primary peak and in most cases higher-order peaks characteristic of the morphology, as indicated with arrows. The sphere-forming LPE/PVCH 6/42 exhibits relatively poor long-range order (a "liquid-like" packing[27] of spherical PVCH domains), as evidenced by the absence of higher-order narrow structure factor peaks; however, the clear minimum (near q = 0.5 nm^{-1}) and maximum (near q = 0.65 nm^{-1}) from the form factor of the molten LPE spheres indicates the expected narrow distribution of sphere diameters.

From the position of the first-order peak q^*, Bragg's law permits the calculation of a characteristic microdomain spacing $d = 2\pi/q^*$. For lamellae, d is the lamellar repeat distance; for cylinders, d is $(3/4)^{1/2}$ times the axis-to-axis separation of adjacent cylinders; and for a body-centered-cubic packing of spheres, d is $(2/3)^{1/2}$ times the center-to-center separation of adjacent spheres. Though the lattice order of our sphere-forming LPE/PVCH is poor, we use this same relation to calculate d, as q^* undergoes at most a minute change as lattice order of the spherical microdomains develops.[28] From these microdomain spacings, the polymers' known LPE weight fractions w_{LPE}, and the melt densities at 140 °C (0.784 and 0.920 g/cm^3 for LPE and PVCH, respectively[29]), we can calculate the sphere diameter D_S, cylinder diameter D_C, or LPE layer thickness L_E for each polymer in the melt; these values are given in Table 1.

When the specimens are cooled to room temperature (black curves in Figure 3a−c), the primary peak position remains essentially unchanged from that in the melt; similarly, the primary peak does not move significantly when the crystallized specimen is heated to slightly below the peak melting temperature (blue curves). This constancy of the peak position is a clear indication that the glassy PVCH domains are not disrupted by crystallization. Nonetheless, major changes in each SAXS pattern occur upon LPE crystallization. The primary peak diminishes greatly in intensity, due to the increase in the average electron density within the LPE domains; the electron densities follow the order ρ^e(LPE,xtal) > ρ^e(PVCH) > ρ^e(LPE,amorph). On the basis of room-temperature mass densities of 1.000,[30] 0.951,[31] and 0.855[32] g/cm^3 for these three components, an electron density match is calculated at an LPE weight fraction crystallinity of 0.73.

While the primary peak intensity decreases upon crystallization, the intensity at higher q increases due to additional electron density heterogeneity associated with the crystals which form within the LPE domains.[15] While the complexity of the SAXS patterns in Figure 3 does not permit an unambiguous determination of the size or shape of the LPE crystals, the fact that the microdomain morphology is preserved clearly indicates that the LPE crystals must fit within the spaces defined by the LPE microdomains in the melt. Thus, we envision "disk-like" crystals within the sphere-forming LPE/PVCH 6/42, where both the thickness and diameter of the crystal must be less than the sphere diameter, and "ribbon-like" crystals within the cylinder-forming LPE/PVCH 15/23, where the crystals can be as long as the cylinders, but where their thickness and width must be less than the cylinder diameter. For the lamellae-forming specimens, we anticipate that the crystal stems will lie parallel to the lamellar interface, based on the work of Douzinas et al.[10] and Hamley et al.,[11] thereby forming ribbon-like LPE crystals which are stacked orthogonally to the layered PVCH and LPE microdomains; indeed, our experimental observations (presented below) confirm this expectation. Note that

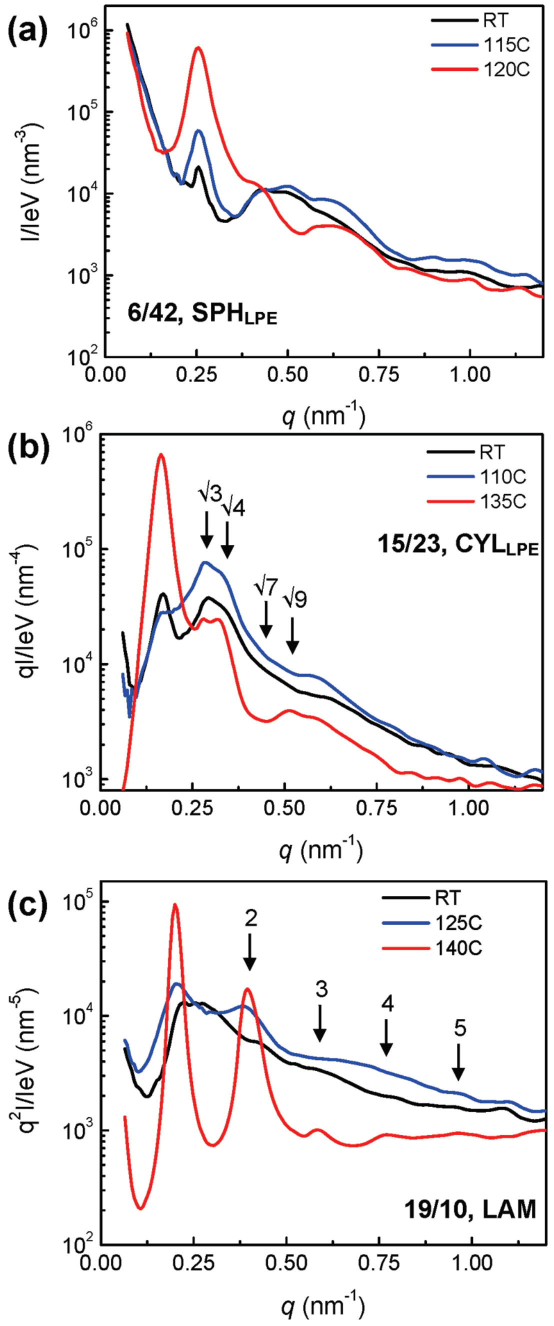

Figure 3. 1D SAXS patterns for three representative LPE/PVCH diblocks in the melt (red), at room temperature (black), and upon reheating to just below the melting temperature (blue). Numbered arrows indicate the expected positions of higher-order peaks, based on the lattice symmetry and the position of the primary reflection. (a) LPE/PVCH 6/42, which forms a liquid-like packing of LPE spheres. (b) LPE/PVCH 15/23, which forms a hexagonal packing of LPE cylinders. (c) LPE/PVCH 19/10, which forms an alternating lamellar structure.

throughout our discussion we use "thickness" to refer to the dimension of the crystal between chain fold surfaces. In the folded-chain lamellae typically formed by crystallizing homopolymers, this is the "short dimension" of the crystal, i.e., the thickness is far less than the other two lateral dimensions. For disk-like or ribbon-like crystals, however, one or both of the lateral dimensions could be similar to or even smaller than the thickness, a possibility which is further explored below.

On the basis of the peak melting temperatures listed in Table 1, a crystal thickness t_c can be calculated. For LPE homopolymer, the data of Bair et al.[33] on solution-crystallized LPE single-crystal mats yield the following relationship between T_m and t_c:

$$T_m = 141.9\ °\mathrm{C} - (168\ °\mathrm{C} - \mathrm{nm})/t_c \qquad (1)$$

Bair et al. measured T_m by DSC on heating at 10 °C/min (as in our experiments), on polyethylene single crystals lightly cross-linked to prevent thickening during the DSC scan. The form of eq 1 corresponds to that of the Gibbs–Thomson equation for plate-like crystals of large lateral dimension,[34] with an equilibrium melting temperature T_m^0 of 141.9 °C. Taking the melting enthalpy[35] ΔH = 277 J/g and the crystal density[30] ρ_c = 0.964 g/cm^3 (at 126 °C, near T_m), the coefficient of 168 °C − nm ($= 2\gamma_e T_m^0/(\rho_c \Delta H)$, with T_m^0 in absolute units) yields a fold surface energy γ_e = 55 erg/cm^2. For crystals of finite lateral dimension, we can rewrite the Gibbs–Thomson equation as follows:

$$\text{disk-like}: \quad (1 - T_m/T_m^0)(\Delta H/\rho_c) = 2\gamma_e/t_c + \gamma_s/D_x \qquad (2a)$$

$$\text{ribbon-like}: \quad (1 - T_m/T_m^0)(\Delta H/\rho_c) = 2\gamma_e/t_c + 2\gamma_s/W_x \qquad (2b)$$

where T_m and T_m^0 are in absolute units, D_x is the diameter of a disk-like crystal (modeled as a right circular cylinder), W_x is the width of a ribbon-like crystal (modeled with a rectangular cross section), and γ_s is the "side" surface energy of the crystal, i.e., the surface along which the crystal stems add. On the basis of the assessment of Hoffman and Miller,[36] we take γ_s = 11.8 erg/cm^2. Note that if the second term in the right-hand side of either eq 2a or 2b is dropped, the Gibbs–Thomson equation for plate-like crystals of large lateral extent is recovered.

From the weight fraction crystallinity in the LPE block measured by DSC, listed as $w_{c,\mathrm{LPE}}$ in Table 1, and using densities for amorphous[29] and crystalline[30] LPE near the melting point (126 °C) of 0.792 and 0.964 g/cm^3, we solve for the values of t_c and D_x which satisfy eq 2a for LPE/PVCH 6/42 or the values of t_c and W_x which satisfy eq 2b for LPE/PVCH 10/27 and 15/23, on the assumption of one crystal per domain. These results are also listed in Table 1. For LPE/PVCH 6/42, 15/23, and 10/27, the crystal thicknesses so calculated are only 6–16% larger than the values obtained by ignoring the finite lateral size of the crystals (i.e., dropping the last term in eqs 2a and 2b).

For the lamellar samples, there is an ambiguity in determining the crystal width W_x, since there are undoubtedly multiple crystals per LPE lamella. As shown directly below, the LPE crystals in our LPE/PVCH diblocks stack orthogonally to the LPE/PVCH lamellae.[10,11] Clearly, the width of the crystal cannot be greater than L_E; however, since the degrees of crystallinity (see Table 1) are ~0.6, it is entirely possible that there is a layer of amorphous LPE adjacent to the LPE–PVCH domain interface, such that $W_x < L_E$, compensated by a higher linear crystallinity along the midplane of the LPE lamella to yield the overall LPE crystallinity measured by DSC. For purposes of calculation in Table 1, we set $W_x = L_E$ for the lamellar samples; however, we recognize that this is an upper bound on W_x, and therefore the value of t_c extracted from eq 2b is a lower bound. Since the "side energy" term in eq 2b is always much smaller than the "fold energy" term ($\gamma_e/\gamma_s \approx 5$), uncertainty in W_x does not produce a comparably large uncertainty in t_c, as will be discussed further below.

For LPE/PVCH 25/7, where the PVCH blocks form cylinders in an LPE matrix, t_c was calculated assuming plate-like crystals (i.e., omitting the last term in eq 2b), because the cylinders do not impose a direct limitation on the lateral extent of the crystals. Note, however, that the maximum thickness of a plate-like crystal wedged into a hexagonal lattice is equal to ($d - D_C$), or only 13.1 nm for LPE/PVCH 25/7, whereas t_c calculated from T_m is larger, 14.6 nm. Indeed, even the edge-to-edge separation between adjacent cylinders is only 17.5 nm. This implies some undulation of the crystal thickness, with the crystals being thinner at the "nips" between cylinders, and thicker in the regions in between. Such a thickness modulation would also be necessary for the LPE matrix to reach its measured crystalline fraction of 0.74. Some indirect support for this idea comes from the breadth of the DSC melting endotherm; for LPE/PVCH 25/7, the breadth (full width at half-maximum) is 11 °C, while for LPE/PVCH 10/27 and 15/23, it is only 7 °C, despite the lower T_m of the latter two.

For the diblocks forming spheres or cylinders of LPE, t_c could be increased only slightly by variations in the thermal history, such as annealing just below the melting point; such thermal treatments could increase t_c by at most 20%, since t_c is directly limited by the dimensions of the spherical or cylindrical microdomains which house the crystal. For lamella-forming diblocks, by contrast, t_c could be increased greatly by annealing; this point will be returned to below.

Coupling between Microdomain and Crystal Orientations. Previous studies of hPBd/PVCH diblocks have shown that the presence of lamellar or cylindrical microdomains can induce a strong orientation of the crystals which form nearby.[2] For PE, the fast-growth direction is the *b*-axis; thus, in cylinder-forming block copolymers, the PE *b*-axis aligns preferentially with the cylinder axis, as crystals grow unhindered only when growing parallel to the cylinders.[9] Similarly, in lamella-forming block copolymers, both the *b*-axis and the *c*-axis preferentially lie in the plane of the lamellae, producing an orientation of the orthorhombic PE unit cell wherein the *a*-axis lies parallel to the lamellar normal.[10,11] Thus, by incorporating PE into suitable block copolymers and aligning the microdomains prior to crystallization, one can produce macroscopic specimens with strong *a*-axial or *b*-axial symmetry to complement the *c*-axial texture produced in fibers; we confirm below that these textures can be achieved in our LPE/PVCH diblocks. Moreover, compared with hPBd/PVCH diblocks, the high PE crystallinity in LPE/PVCH diblocks should lead to a tighter orientational coupling between the LPE crystals and the cylindrical or lamellar microdomains. To test this idea, specimens were aligned in planar extensional flow in a lubricated channel die,[24,25] where the extensional axis is denoted "flow direction" (FD), the compressional axis "load direction" (LD), and the neutral direction "constraint direction" (CD). Previous investigations[24,25] have shown that lamellar specimens generally align with the lamellar normals parallel to LD, while cylinder-forming materials align the cylinder axes along FD.

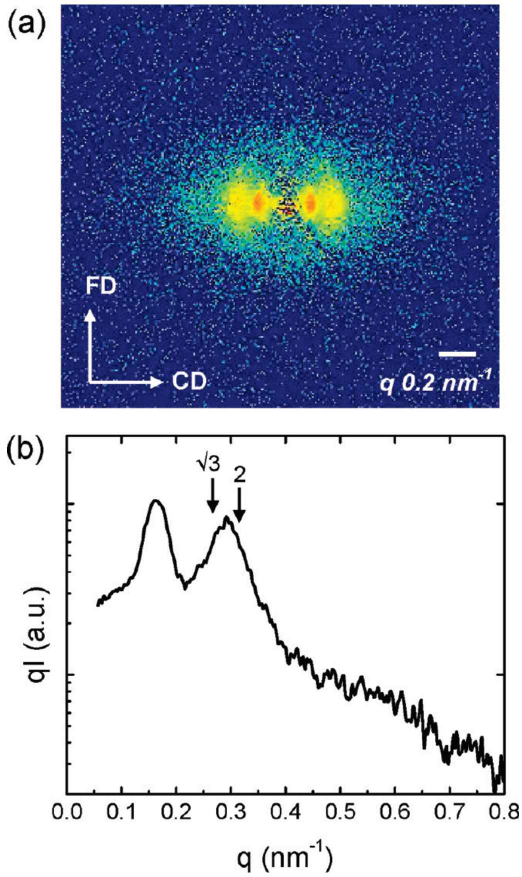

Figure 4. (a) Room temperature 2D SAXS pattern for LPE/PVCH 15/23 with beam along LD; FD is vertical, cylinder axes are aligned with FD. (b) 1D pattern (equatorial cut, ±25° sector across equator) showing a peak at $q^* = 0.161\ \mathrm{nm}^{-1}$ and a broader peak encompassing $\sqrt{3}q^*$ and $2q^*$.

Consider first the case where LPE crystallization is confined within cylinders. Figure 4a shows SAXS data at room temperature for LPE/PVCH 15/23, demonstrating the expected strong orientation of the cylinder axes along FD. Figure 4b shows a 1D trace of the SAXS pattern taken along the equator, showing the first-order peak at $q^* = 0.161\ \mathrm{nm}^{-1}$ and a broader peak spanning the range for the higher-order reflections at $\sqrt{3}q^*$ and $2q^*$ expected for a well-ordered hexagonal lattice. The scattering in this q-region is augmented and blurred by the additional electron density heterogeneity resulting from PE crystals within the cylinders,[15] as in Figure 3b. Figure 5a shows the corresponding 2D WAXS data for oriented LPE/PVCH 15/23, with the beam along CD, i.e., perpendicular to the cylinder axes. The two-spot equatorial character of the (200) reflection, and the four-spot character of the (110) reflection, with a split angle across the equator $\sigma = 114°$, correspond to a strong orientation of the LPE *b*-axis along FD (i.e., along the cylinder direction; calculated $\sigma = 115.7°$). Figure 5b shows the azimuthal traces for the (110) and (200) reflections, along with the (200) and (210) reflections, which are not typically visible in hPBd-based materials. The azimuthal locations of all these reflections ((200) on the meridian; (210) split across the equator with $\sigma = 77°$) confirm the *b*-axial orientation of the specimen; moreover, the exceptionally narrow azimuthal spread of all reflections (full width at half maximum ≈ 15° for all), compared with analogous hPBd/PVCH diblocks, indicates a very tight coupling between the orientation of the crystals and the microdomains. For the converse case where LPE forms the matrix surrounding the PVCH cylinders, one again expects alignment of the fast-growth *b*-axis parallel to the cylinder axis, as previously found for hPBd-based diblocks.[37,38] Figure 6 shows 2D SAXS data for LPE/PVCH 25/7, both in the melt and in the crystallized solid, again confirming an alignment of the cylinder axes along FD which is fully retained upon crystallization. Figure 7 shows the complementary room-temperature 2D WAXS data, where with the beam along LD (Figure 7a) the (110) split angle $\sigma = 118°$ and the equatorial position of the (200) reflection again confirm strong alignment of the *b*-axis parallel to that of

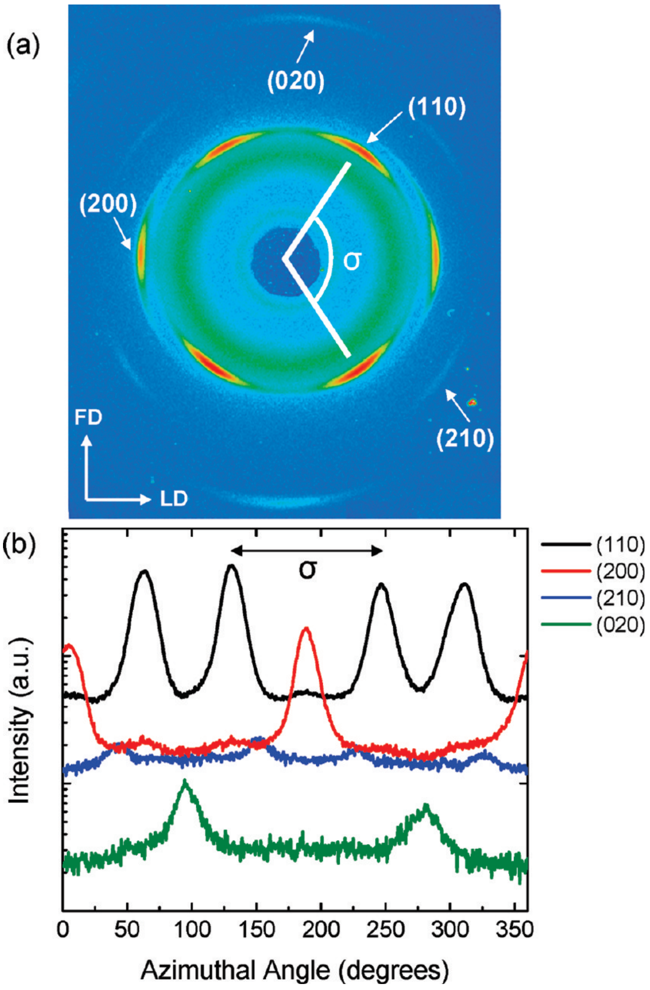

Figure 5. (a) 2D WAXS pattern for LPE/PVCH 15/23, with the incident beam along CD. (b) Azimuthal intensity profiles; locations of all reflections confirm alignment of the *b*-axis with the cylinder axis (along FD, on the meridian).

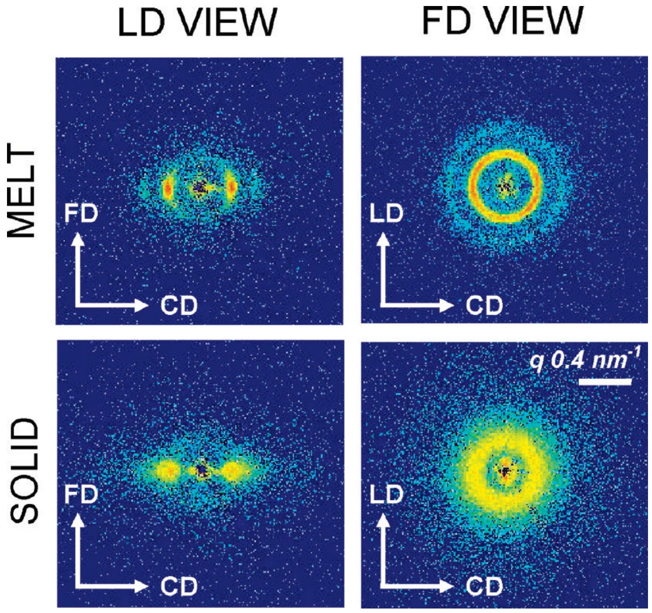

Figure 6. SAXS patterns for flow-aligned LPE-PVCH 25/7. Top row: melt, 160 °C. Bottom row: room temperature, after LPE crystallization. Left column: beam along LD. Right column: beam along FD.

the cylinders. But the strength of the *b*-axial alignment is even more evident when the beam is pointed down FD, as in Figure 7b: in this view, due to rotational isotropy around the cylinder axis, both the (110) and (200) reflections appear as rings, but the (200) reflection is 3 times *more intense* than the (110) reflection, whereas for isotropic PE, the (200) is at least 2 times *weaker* than the (110). Note that if the *b*-axis were perfectly aligned along FD, then neither the (110) nor the (200) reflection would meet the Bragg condition with the beam along FD; however, a tilt of only 12° is required for the (200) to meet the Bragg condition, while the (110) requires a tilt of over 45°.

Consider next crystallization within lamellae, a case studied for hPBd/PVCH diblocks by Hamley.[11] Parts a and b of Figure 8 show 2D SAXS patterns for LPE/PVCH 15/18 in the melt and the solid state, respectively. The melt pattern in Figure 8a confirms the expected orientation of the lamellar normals along the channel die's LD, since narrow arcs are observed along FD in a q ratio of 1:2:3. When the LPE block crystallizes, the narrow meridional arcs are retained, though the primary peak is reduced in intensity due to the aforementioned reduction in electron density contrast between LPE and PVCH.

More notably, two intense but comparatively diffuse bars of intensity appear on the equator, reflecting the stacking of the LPE crystallites orthogonal to the LPE/PVCH domain layering, as depicted schematically in Figure 8c and analyzed previously by Hamley[11] for hPBd/PVCH. However, unlike hPBd/PVCH—where the crystallites are limited[15] to an average thickness of ca. 5 nm by the ethyl branch defects in hPBd—in LPE, there is no direct limit to the thickness of the crystallites. Indeed, it is easily possible for the LPE crystallites to be thicker than the LPE domains which contain them, since the two are stacked orthogonally; we will return to this point below.

Crystal Thicknesses within Lamellar Microdomains. The orthogonality of the scattering between the microdomains and the crystals in lamellar samples allows for a direct measurement of t_c by SAXS. An equatorial cut across Figure 8b shows a peak at $q^* = 0.32$ nm^{-1}, corresponding to a crystal–amorphous repeat distance $d_c = 19.6$ nm. A specimen with the same thermal history (cooled in the hot press used for channel die alignment) shows a DSC peak $T_m = 125.1$ °C; by eq 2b, with $W_x = L_E = 13.4$ nm, this yields $t_c = 12.0$ nm. The measured enthalpy in the same DSC scan translates to $w_{c,LPE} = 0.58$, hence, a volume fraction crystallinity $\phi_c = 0.54$ and a crystal thickness $t_c = \phi_c d_c = 11$ nm. However, note that this calculation assumes $W_x = L_E$, i.e., that the LPE crystals can grow right up to the LPE/PVCH interface. If instead we postulate an exclusion layer of 1.0 nm next to the interface, such that $W_x = 11.4$ nm, we then calculate $t_c = 12.4$ nm by eq 2b, along with a linear $\phi_c = 0.63$ down the domain center, which yields a SAXS $t_c = \phi_c d_c = 12.4$ nm. With such an exclusion layer present, the t_c values derived from SAXS and DSC are brought into perfect agreement—at a value of t_c quite close to that determined by DSC without the assumption of such an exclusion layer. We emphasize that this ambiguity exists only for the lamellar morphology, where the number of crystals per microdomain is indeterminate; for polymers containing spheres or cylinders of LPE, both t_c and D_x (or W_x) are determined directly from eq 2a (or eq 2b), using the measured value of $w_{c,LPE}$, provided only one crystal is present per domain.

Figure 9a shows the complementary WAXS data (CD view) for LPE/PVCH 15/18. For perfect alignment of the *a*-axes with the lamellar normals (along LD, vertical), the (200) reflection should lie on the meridian and the (020) on

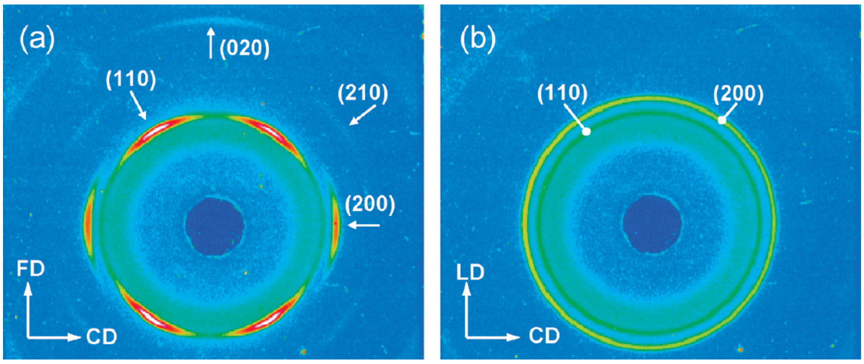

Figure 7. 2D WAXS patterns for LPE/PVCH 25/7 at room temperature. (a) Beam along LD. (b) Beam along FD.

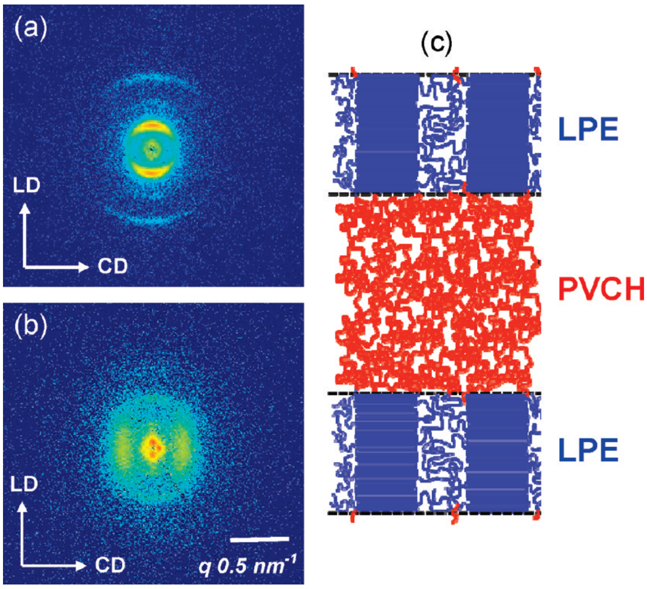

Figure 8. 2D SAXS patterns for LPE/PVCH 15/18, beam along FD, LD vertical: (a) melt, 150 °C, (b) room temperature. (c) Schematic of the corresponding orientation of the LPE/PVCH lamellae and of the LPE crystals within the lamellae; one lamellar repeat, plus an additional LPE layer, shown.

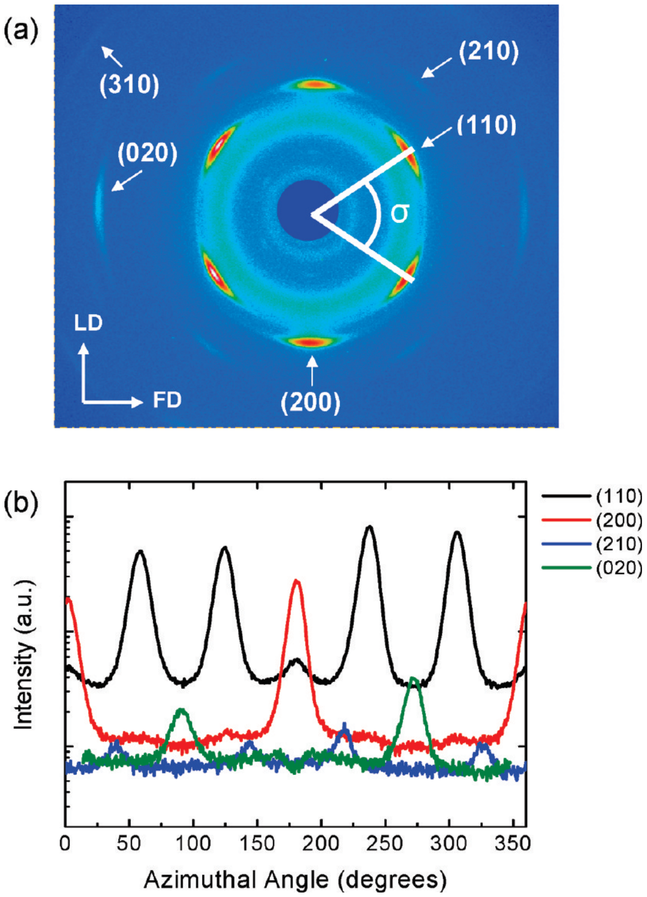

Figure 9. (a) 2D WAXS pattern for LPE/PVCH 15/18 at room temperature, with the incident beam along CD. (b) Azimuthal intensity profiles, confirming *a*-axial orientation.

the equator, while the (110) reflection should be split across the equator[11] with $\sigma = 68.8°$. The observed positions of all three reflections (with a measured $\sigma = 67°$ for the (110) reflection) confirm the *a*-axial orientation. The azimuthal intensity distributions plotted in Figure 9b show the same narrow breadth (full width at half-maximum $< 15°$) observed in Figure 5b for the cylinder-forming LPE/PVCH 15/23, again indicating a much tighter orientational coupling between the crystallites and the microdomains than in the hPBd/PVCH case.[11]

Since the chain axes and the lamellar normals are perpendicular, as schematized in Figure 8c, confinement of the LPE to lamellae does not impose a direct limitation on the thickness of the LPE crystals. An intriguing question, then, is: what *does* determine the thickness of the crystals in lamellar semicrystalline diblocks? For homopolymers, of course, the crystal thickness is typically set kinetically, via the crystallization history, with crystallization at shallower undercoolings leading to thicker crystals. For LPE, crystals can also thicken substantially by annealing at temperatures below the melting point.[39] But while in homopolymers, crystals can thicken essentially without limit (up to the fully extended length of the chain, in principle), in block copolymers there must be an upper limit imposed by the attachment of the block junction to the interface, with an average area per chain[40] which is established in the melt, prior to vitrification.

For the thermal histories we are able to practically access, we find that the LPE crystals in our LPE/PVCH diblocks are still in a regime where their thicknesses are kinetically limited. This is most easily tracked via the peak crystal melting point T_m determined by DSC on heating, following a prescribed thermal history. Figure 10 shows that, for lamellar diblocks, the peak T_m increases with a 1 h anneal below the melting point; moreover, the higher the annealing temperature, the greater the increase in T_m following annealing. Of course, if the annealing temperature T_a exceeds the melting point in the quenched specimen, then no crystals are

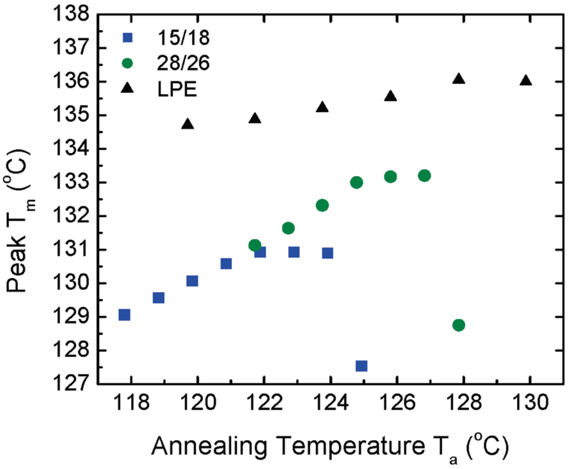

Figure 10. Peak LPE melting temperature T_m (DSC heating, 10 °C/min) following a 1 h anneal at T_a, for two lamellar diblocks (LPE/PVCH 15/18 and 28/26) and an LPE homopolymer (20 kg/mol).

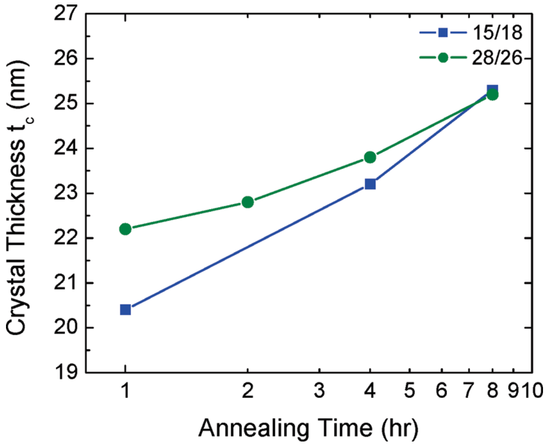

Figure 11. Crystal thickness t_c, determined via eq 2b with $W_x = L_E$, as a function of annealing time for the two lamellar diblocks of Figure 10. Annealing temperature was 123 °C for LPE/PVCH 15/18 and 126 °C for LPE/PVCH 28/26.

present during annealing and the subsequently measured T_m will be much reduced; this dropoff is evident in Figure 10 at just below 125 °C for LPE/PVCH 15/18 and 128 °C for LPE/PVCH 28/26.[41] Prior to this dropoff, T_m for the block copolymers progressively approaches, but does not quite reach, that for the LPE homopolymer[18] (M_n = 20 200 g/mol, PDI = 1.07). However, much of this difference in T_m can be attributed to the additional melting point depression contributed by the finite W_x of the crystals in the lamellar diblocks; for the homopolymer, the value of T_m = 136 °C achieved at the higher values of T_a translates to t_c = 28 nm via eq 1. By comparison, the value of T_m = 133.1 °C achieved for LPE/PVCH 28/26, following a 1 h anneal at T_a = 126 °C, translates to t_c = 22 nm by eq 2b, with W_x set equal to L_E (thus yielding a lower bound on t_c). In Figure 10, the T_m values for each diblock appear to plateau before reaching the dropoff. To investigate whether these plateau values represent the diblock's limiting (equilibrium) melting point, we annealed each diblock for more extended periods, at a value of T_a within the plateau region in Figure 10 (at T_a = 123 °C for LPE/PVCH 15/18 and 126 °C for LPE/PVCH 28/26). However, T_m continued to steadily increase with annealing time, indicating that the crystal thicknesses remain kinetically limited. The measured T_m values were converted to t_c via eq 2b, assuming $W_x = L_E$, and are presented in Figure 11. The crystal thickness appears to grow roughly linearly with the logarithm of annealing time, as previously documented for LPE homopolymer.[39] While we do expect, by the considerations outlined above, that a limiting value of t_c should eventually be approached, Figure 11 indicates that this thickness must exceed 25 nm for these diblocks and that exceedingly long annealing times would be required to reach this limiting value. Figure 11 also clearly reflects that the lamellar microdomains do not impose a direct constraint on the crystal thickness, as schematized in Figure 8c; for LPE/PVCH 15/18, t_c after annealing is nearly twice L_E; i.e., the crystals are nearly twice as thick as they are wide, even though they have still not reached their limiting thickness.

Conclusions

In hPBd/PVCH diblocks, the ethyl branches in the hPBd block limit the crystal thickness to 5 nm, far below the typical microdomain width, so even when crystallization is confined by a preexisting microdomain structure, the crystal thickness is not impacted. Eliminating these ethyl branches, as in LPE/PVCH diblocks, directly limits the crystal thickness when LPE is confined to spheres or cylinders. This limitation is clearly reflected in the crystal melting temperature; combining the melting point and melting enthalpy (LPE crystallinity) from DSC permits assessment of both the thickness and lateral extent of the disk-like LPE crystals which form within spheres and the ribbon-like crystals which form within cylinders. Confinement of LPE between glassy PVCH cylinders also limits the crystal thickness, though with local variations reflecting the distance between LPE/PVCH interfaces. When confined within lamellae, LPE crystals stack orthogonally to the LPE/PVCH microdomain layering, so that the PVCH domains place a direct limitation on only the lateral extent of the crystals, not on their thickness. Consequently, LPE crystals confined within lamellae can thicken upon annealing, ultimately developing thicknesses which can significantly exceed the limited crystal width. Confinement within lamellae, or within or between cylinders, imparts a strong orientation of the crystals with respect to the LPE/PVCH interface. Therefore, alignment of the confining mesophase structure (by melt processing) imparts a strong orientation to the crystals which form subsequently. Macroscopic specimens have an *a*-axial texture of the orthorhombic LPE crystals (in lamellae) or *b*-axial texture (within or between cylinders), which complement the *c*-axial texture typically achieved by melt spinning of semicrystalline homopolymers.

Acknowledgment. This work was supported by the National Science Foundation, through the Polymers Program (DMR-0505940) and through a Graduate Research Fellowship to S.B.M. Design, construction, and acquisition of the Molecular Metrology SAXS system were supported through the National Science Foundation, Instrumentation for Materials Research Program (DMR-0215578).

Note Added after ASAP Publication. This article was released ASAP on November 17, 2009, with minor errors in the text. The correct version was posted on November 30, 2009.

References and Notes

(1) Hamley, I. W. *Adv. Polym. Sci.* **1999**, *148*, 113–137.
(2) Loo, Y.-L.; Register, R. A. In *Developments in Block Copolymer Science and Technology*; Hamley, I. W., Ed.; John Wiley & Sons, Ltd.: Chichester, 2004; pp 213–243.
(3) Müller, A. J.; Balsamo, V.; Arnal, M. L. *Adv. Polym. Sci.* **2005**, *190*, 1–63.

(4) Lotz, B.; Kovacs, A. J. *Polym. Prepr.* (*Am. Chem. Soc., Div. Polym. Chem.*) **1969**, *10* (2), 820–825.

(5) Loo, Y.-L.; Register, R. A.; Ryan, A. J. *Phys. Rev. Lett.* **2000**, *84*, 4120–4123.

(6) Reiter, G.; Castelein, G.; Sommer, J.-U.; Röttele, A.; Thurn-Albrecht, T. *Phys. Rev. Lett.* **2001**, *87*, 226101.

(7) Zhu, L.; Cheng, S. Z. D.; Calhoun, B.; Ge, Q.; Quirk, R. P.; Thomas, E. L.; Hsiao, B. S.; Yeh, F.; Lotz, B. *J. Am. Chem. Soc.* **2000**, *122*, 5957–5967.

(8) Sun, Y.-S.; Chung, T.-M.; Li, Y.-J.; Ho, R.-M.; Ki, B.-T.; Jeng, U.-S. *Macromolecules* **2007**, *40*, 6778–6781.

(9) Quiram, D. J.; Register, R. A.; Marchand, G. R.; Adamson, D. H. *Macromolecules* **1998**, *31*, 4891–4898.

(10) Douzinas, K. C.; Cohen, R. E. *Macromolecules* **1992**, *25*, 5030–5035.

(11) Hamley, I. W.; Fairclough, J. P. A.; Terrill, N. J.; Ryan, A. J.; Lipic, P. M.; Bates, F. S.; Towns-Andrews, E. *Macromolecules* **1996**, *29*, 8835–8843.

(12) Falk, J. C.; Schlott, R. J. *Angew. Makromol. Chem.* **1972**, *21*, 17–23.

(13) Weimann, P. A.; Hajduk, D.A.; Chu, C.; Chaffin, K.A.; Brodil, J. C.; Bates, F. S. *J. Polym Sci., Part B: Polym. Phys.* **1999**, *37*, 2053–2068.

(14) Peacock, A. J. *Handbook of Polyethylene: Structures, Properties, and Applications*; Marcel Dekker, Inc.: New York, 2000.

(15) Loo, Y.-L.; Register, R. A.; Ryan, A. J.; Dee, G. T. *Macromolecules* **2001**, *34*, 8968–8977.

(16) Loo, Y.-L.; Register, R. A.; Ryan, A. J. *Macromolecules* **2002**, *35*, 2365–2374.

(17) Myers, S. B.; Register, R. A. *Macromolecules* **2008**, *41*, 5283–5288.

(18) Trzaska, S. T.; Lee, L.-B. W.; Register, R. A. *Macromolecules* **2000**, *25*, 9215–9221.

(19) Register, R. A.; Bell, T. R. *J. Polym. Sci., Part B: Polym. Phys.* **1992**, *30*, 569–575.

(20) Huang, T. C.; Toraya, H.; Blanton, T. N.; Wu, Y. *J. Appl. Crystallogr.* **1993**, *26*, 180–184.

(21) Shenfil, L.; Danielson, W. E.; DuMond, J. W. M. *J. Appl. Phys.* **1952**, *23*, 854–859.

(22) Gabriel, A.; Dauvergne, F. *Nucl. Instrum. Methods* **1982**, *201*, 223–224.

(23) Dean, D. M.; Rebenfeld, L.; Register, R. A.; Hsiao, B. S. *J. Mater. Sci.* **1998**, *33*, 4797–4812.

(24) Scott, D. B.; Waddon, A. J.; Lin, Y.-G.; Karasz, F. E.; Winter, H. H. *Macromolecules* **1992**, *25*, 4175–4181.

(25) Lee, H. H.; Register, R. A.; Hajduk, D. A.; Gruner, S. M. *Polym. Eng. Sci.* **1996**, *36*, 1414–1424.

(26) Ruokolainen, J.; Fredrickson, G. H.; Kramer, E. J.; Ryu, C. Y.; Hahn, S. F.; Magonov, S. N. *Macromolecules* **2002**, *35*, 9391–9402.

(27) Kinning, D. J.; Thomas, E. L. *Macromolecules* **1984**, *17*, 1712–1718.

(28) Adams, J. L.; Quiram, D. J.; Graessley, W. W.; Register, R. A.; Marchand, G. R. *Macromolecules* **1996**, *29*, 2929–2938.

(29) Fetters, L. J.; Lohse, D. J.; Richter, D.; Witten, T. A. *Macromolecules* **1994**, *27*, 4639–4647.

(30) Swan, P. R. *J. Polym. Sci.* **1962**, *56*, 403–407.

(31) Reichart, G. C. Ph.D. Thesis, Princeton University, **1997**.

(32) Stehling, F. C.; Mandelkern, L. *Macromolecules* **1970**, *3*, 242–252.

(33) Bair, H. E.; Huseby, T. W.; Salovey, R. *Polym. Prepr.* (*Am. Chem. 718 Soc., Div. Polym. Chem.*) **1968**, *9* (1), 795–805; Crist, B. *J. Polym. Sci., Part B: Polym. Phys.* **2007**, *45*, 3231–3236.

(34) Strobl, G. *The Physics of Polymers*, 3rd ed.; Springer-Verlag: Berlin, 2007; p 192.

(35) Wunderlich, B.; Dole, M. *J. Polym. Sci.* **1957**, *24*, 201–213.

(36) Hoffman, J. D.; Miller, R. L. *Polymer* **1997**, *38*, 3151–3212.

(37) Park, C.; De Rosa, C.; Fetters, L. J.; Thomas, E. L. *Macromolecules* **2000**, *33*, 7931–7938.

(38) Loo, Y.-L.; Register, R. A.; Adamson, D. H. *Macromolecules* **2000**, *33*, 8361–8366.

(39) Fischer, E. W.; Schmidt, G. F. *Angew. Chem., Int. Ed. Engl.* **1962**, *1*, 488–499.

(40) Winey, K. I.; Thomas, E. L.; Fetters, L. J. *Macromolecules* **1991**, *24*, 6182–6188.

(41) Comparison of Figure 10 and Table 1 shows that, for each diblock, the dropoff in Figure 10 occurs ~2 °C below the peak T_m given in Table 1. This is due to thermal lag in the DSC on heating at 10 °C/min, such that the actual specimen temperature is slightly below that recorded, leading to correspondingly high values of T_m in Table 1. By using the T_m values of Bair et al.,[33] which were also determined by DSC at 10 °C/min, the effect of this thermal lag on the calculated values of crystal thickness is accounted for. Alternatively, SAXS measurements of t_c on slow heating through T_m have yielded[42] $T_m^0 = 141.2$ °C, with a slope of -132 °C-nm, for uncrosslinked melt-crystallized LPE. These parameters are similar to those quoted in eq 1, with the slightly shallower slope yielding a slightly smaller t_c for a given T_m.

(42) Cho, T. Y.; Heck, B.; Strobl, G. *Colloid Polym. Sci.* **2004**, *282*, 825–832.